Nano Energy 68 (2020) 104301

Contents lists available at ScienceDirect

Nano Energy

journal homepage: http://www.elsevier.com/locate/nanoen

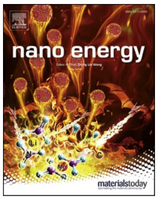

Boosting the alkaline hydrogen evolution of Ru nanoclusters anchored on B/N–doped graphene by accelerating water dissociation

Shenghua Ye [a,1], Feiyan Luo [a,1], Tingting Xu [a,1], Pingyu Zhang [a,**], Hongdong Shi [a], Shiqi Qin [a], Jiaping Wu [a], Chuanxin He [a], Xiaoping Ouyang [d], Qianling Zhang [a,***], Jianhong Liu [a,c,****], Xueliang Sun [b,*]

[a] *College of Chemistry and Environmental Engineering, Shenzhen University, Shenzhen, 518060, PR China*
[b] *Department of Mechanical and Materials Engineering, University of Western Ontario, London, Ontario, N6A 5B9, Canada*
[c] *Shenzhen Eigen–Equation Graphene Technology Co. Ltd., Shenzhen, 518000, PR China*
[d] *School of Materials Science and Engineering, Xiangtan University, Xiangtan, 411105, PR China*

ARTICLE INFO

Keywords:
Ru
B/N–doped graphene
Water dissociation
Hydrogen evolution reaction

ABSTRACT

The development of the hydrogen evolution reaction (HER) in alkaline electrolyte is highly desirable but is hindered by sluggish water dissociation and the high cost of Pt–based catalysts. In this study, a facile pyrolyzation method is proposed for synthesizing the Ru nanoclusters (NCs) anchored on B/N–doped graphene (BNG) (denoted as Ru NCs/BNG). During the pyrolyzation, boron was doped into graphene and facilitated the formation of ultra–small Ru NCs with a diameter of 0.5–1 nm. The electronic interaction between B and Ru NCs accelerated the cleavage of H–OH, altering the HER mechanism and lowering the activation energy of H_2 formation, endowing Ru NCs/BNG with excellent alkaline HER activity, even surpassing that of Pt/C. This study reveals the importance of water dissociation barriers for alkaline HER activity and provides a new strategy for improving the HER catalytic activity.

1. Introduction

Electrochemical water splitting has attracted much attention in recent years because it is not only a promising technology for the development of large–scale hydrogen evolution but also an important reaction in next–generation energy conversion devices such as metal––air batteries and fuel cells [1–5].

Water splitting involves two half–reactions: the hydrogen evolution reaction (HER) at the cathode and the oxygen evolution reaction (OER) at the anode. Most state–of–the–art OER catalysts are only stable in alkaline solution [6], while acidic solutions corrode the devices and often form acidic fog during electrolysis, which is undesirable in the preparation of high–purity hydrogen [7,8]. Due to the above reasons, the HER is more favorable in an alkaline electrolyte. However, most efficient HER catalysts require an acidic electrolyte; thus, exploring HER catalysts that can work efficiently in an alkaline electrolyte is necessary to overcome this issue.

The mechanism of the HER in alkaline solution involves the release of protons from water dissociation, unlike the mechanism in acidic solution, in which protons in solution are directly adsorbed and reduced at catalytically active sites [9–12]. The barrier of water molecule dissociation ($K_w = 1 \times 10^{-14}$, 298 K) slows the HER dynamics in alkaline solution; consequently, the current electrocatalysts show insufficient activity under alkaline conditions, even though for most active catalysts, Pt remains two or three orders of magnitude less efficient than under acidic conditions due to its insufficient catalysis ability toward H–OH bond cleavage [10,13–15]. Herein, the overall HER activity in alkaline solution is governed not only by the intrinsic ability of the catalyst to catalyze H^+ to H_2 (appropriate H binding energy) but also by the kinetics of water molecule dissociation on the interface (low barrier to

---

* Corresponding author.
** Corresponding author.
*** Corresponding author.
**** Corresponding author. College of Chemistry and Environmental Engineering, Shenzhen University, Shenzhen, 518060, PR China.
E-mail addresses: p.zhang6@szu.edu.cn (P. Zhang), zhql@szu.edu.cn (Q. Zhang), liujh@szu.edu.cn (J. Liu), xsun@eng.uwo.ca (X. Sun).
[1] Shenghua Ye, Feiyan Luo and Tingting Xu contribute equally to this work.

https://doi.org/10.1016/j.nanoen.2019.104301
Received 27 September 2019; Received in revised form 31 October 2019; Accepted 14 November 2019

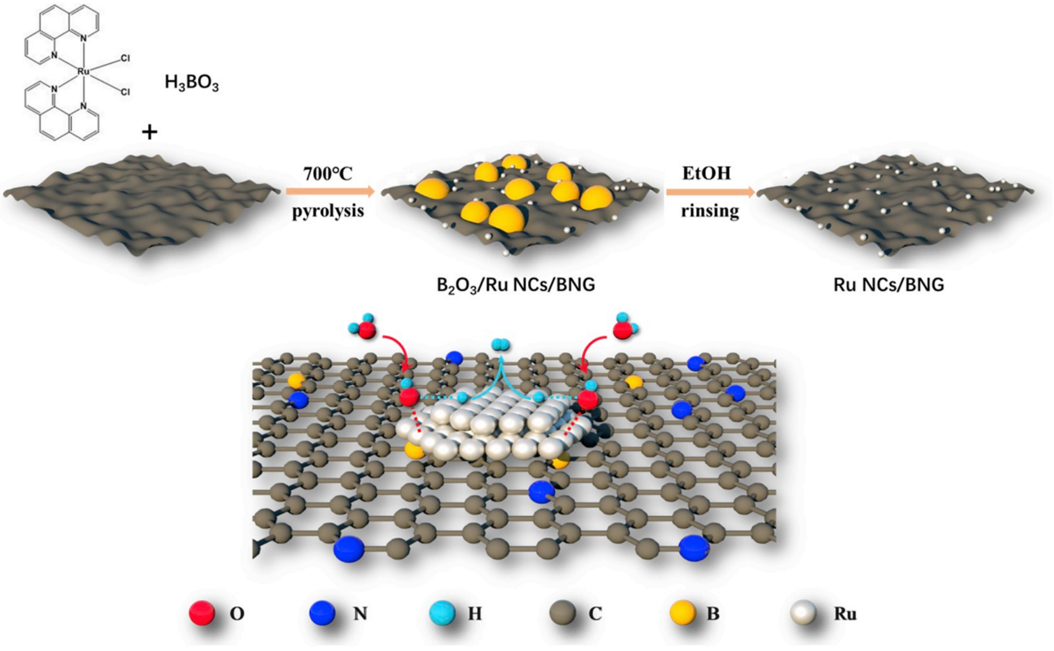

Scheme 1. Synthesis and structure of Ru NCs/BNG.

water dissociation). Therefore, accelerating the water dissociation is a crucial but challenging task in boosting the HER dynamics in alkaline solution.

In this study, Ru nanoclusters (NCs) anchored on B/N–doped graphene (BNG) (denoted as Ru NCs/BNG) were synthesized *via* pyrolyzation of a mixture of Ru $(phen)_2Cl_2$, H_3BO_3, and graphene. H_3BO_3 is crucial to the reaction as it not only prevents the agglomeration of Ru but also provides a boron source to form BNG. Density functional theory (DFT) calculations suggest that the empty 2p orbitals of the boron atoms (the electronic configuration of boron is $1s^22s^22p^1$) can be delocalized to Ru NCs and graphene, facilitating the coordination of the lone−pair electrons in the oxygen atoms of H_2O molecules with Ru NCs, inducing H–OH bond cleavage, and thus accelerating the water dissociation step and boosting the HER dynamics in alkaline solution. Benefiting from the above design, the Ru NCs/BNG present outstanding HER activity with $\eta = 14$ mV at 10 mA cm^{-2}, which is superior to that of 20 wt% Pt/C. Moreover, the price of Ru is only 4% that of Pt, so that Ru NCs/BNG are cheaper but more efficient than Pt with excellent commercial prospects.

2. Experimental section

2.1. Materials

All the chemical reagents used throughout the work were of analytical grade and were used directly without further purification. Single−layer graphene was produced by the Shenzhen Eigen−Equation Graphene Technology Co. Ltd. (Shenzhen, China) *via* liquid sintering of a liquid acrylonitrile homopolymer precursor. $RuCl_3$ was purchased from Aladdin and H_3BO_3 was purchased from the chemical reagent factory of Shenzhen University.

2.2. Catalyst preparation

To prepare Ru NCs/BNG, 12.4 mg of Ru $(phen)_2Cl_2$, 14.6 mg of H_3BO_3, and 10 mg of graphene were dissolved in 50 mL of ethanol to form a uniform dispersion *via* sonication. The ethanol was then evaporated at 60 °C. Subsequently, the resulting powder was heated to 300 °C at a rate of 5 °C/min and held at that temperature for 2 h, then annealed at 700 °C in a N_2 atmosphere for 2 h at a heating rate of 5 °C/min. Eventually, the powder was rinsed several times with water and ethanol and dried at 70 °C to yield Ru NCs/BNG. To prepare Ru NPs/NG, the same procedure was followed without using H_3BO_3.

2.3. Catalyst characterization

The sample morphologies were characterized by TEM (JEM−2010HR and Tecnai F30 S–TWIN), and electron energy loss spectra were recorded on the Tecnai F30 S–TWIN instrument. Chemical−state analysis of the samples was performed by XPS using an ESCALAB 250 X–ray photoelectron spectrometer. All the peaks were corrected using the C 1s line at 284.4 eV as a standard, followed by curve fitting and background subtraction. The percentages of Ru were measured by TGA (TGA, Q–5003061412), and the crystal structures of the samples were characterized by PXRD (Bruker D8 ADVANCE).

2.4. Electrochemical measurements

Electrochemical measurements were performed using a CHI 660E electrochemical analyzer (CH Instruments, Inc., Shanghai) in a standard three−electrode system, using a sample–coated glassy carbon electrode as the working electrode, a graphite rod as the counter electrode, and a saturated calomel electrode (SCE) as the reference electrode. The catalyst loading was 0.707 mg cm^{-2}. In all the measurements, the SCE reference electrode was calibrated with respect to the reversible hydrogen electrode (RHE). In a H_2−saturated electrolyte, $E\ (RHE) = -0.059$ pH V, and $\eta = E\ (RHE) - E\ (electrode) - E\ (SCE)$. LSV measurements were conducted in the electrolyte at a scan rate of 2 mV s^{-1}. Cyclic voltammetry was performed at a scan rate of 50 mV s^{-1}.

2.5. DFT calculations

First−principles calculations in the framework of DFT, including structures and electronic performances, were performed using the Cambridge Sequential Total Energy Package, known as CASTEP [16]. An exchange−correlation functional under the generalized gradient approximation (GGA) [17] with norm−conserving pseudopotentials and the Perdew–Burke–Ernzerhof functional was adopted to describe the electron–electron interactions [18]. An energy cutoff of 750 eV was used

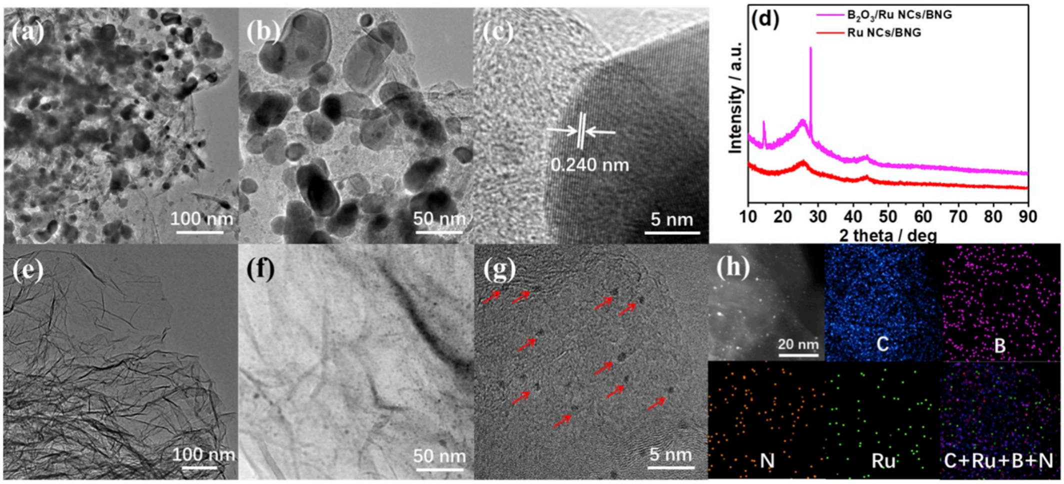

Fig. 1. (a–h) Transmission electron microscopy (TEM) and (c) HR−TEM images of B_2O_3/Ru NCs/BNG; (d) powder X−ray diffraction (PXRD) patterns of B_2O_3/Ru NCs/BNG and Ru NCs/BNG; (e–f) TEM and (g) HR−TEM images of Ru NCs/BNG; and (h) HAADF−STEM image of Ru NCs/BNG and the corresponding elemental mapping results.

and a k−point sampling set of 5 × 5 × 1 was tested for convergence. A force tolerance of 0.01 eV $Å^{-1}$, an energy tolerance of 5.0×10^{-7} eV per atom, and a maximum displacement of 5.0×10^{-4} Å were considered. Each atom in the storage models was allowed to relax to the minimum enthalpy without constraints. The vacuum space along the z direction was set as 15 Å, which is enough space to avoid interactions between the two neighboring images. The Grimme method for DFT−D2 correction was used for all the calculations [19]. A Pt cluster on graphene and a Ru cluster on N/B−co−doped graphene were built, and then the H, H_2O, OH, and H_2 groups were adsorbed on the Pt cluster or N/B−co−doped graphene. A complete linear synchronous transit/quadratic synchronous transit (LST/QST) search protocol, a SCF tolerance of 1.0×10^{-7} eV, and a RMS convergence of 0.02 eV/Å were used for the transition states.

3. Results and discussion

3.1. Morphology and structure

The fabrication of Ru NCs/BNG is depicted in Scheme 1. Firstly, Ru $(phen)_2Cl_2$, H_3BO_3, and graphene were mixed together in ethanol, ethanol was removed by vaporization, and then Ru $(phen)_2Cl_2$ was dispersed on graphene through π–π stacking. Subsequently, the above mixture was pyrolyzed at 700 °C; during this process, Ru $(phen)_2Cl_2$ was reduced to metallic Ru, and H_3BO_3 was transformed to B_2O_3 *via* dehydration. Meanwhile, N and B were doped into graphene during pyrolyzation, forming B_2O_3/Ru NCs/BNG. Eventually, B_2O_3 was completely removed by rinsing with water and ethanol and Ru NCs/BNG were prepared. For comparison, Ru nanoparticles/N−doped graphene (Ru NPs/NG) as a counterpart were synthesized as above but without H_3BO_3. Full details of the materials used in the preparations, synthetic methods, characterization, measurements, calculations, and further data are given in the Experimental section.

As shown in Fig. 1a−b, the transmission electron microscopy (TEM) images of B_2O_3/Ru NCs/BNG show many particles attached to graphene, and the high−resolution TEM (HR–TEM) image in Fig. 1c shows that the particles have good crystallinity with lattice fringes of 0.240 nm, belonging to the (400) facets of B_2O_3. The powder X–ray diffraction (PXRD) pattern of B_2O_3/Ru NCs/BNG shown in Fig. 1d suggests that there are two diffraction peaks at 14.5° and 27.9°, originating from diffraction from B_2O_3 (PDF−#06–0297), and the two broad peaks at 26° and 43° originate from graphene. When B_2O_3/Ru NCs/BNG were rinsed with water and ethanol, the diffraction peaks of B_2O_3 completely disappeared, as shown in Fig. 1d, indicating its removal of B_2O_3. Moreover, there were no diffraction peaks for Ru, suggesting that small metallic Ru clusters were formed. The TEM images of Ru NCs/BNG in Fig. 1e suggest that all the B_2O_3 particles were removed after rinsing with water and ethanol, with no particles being observed in the low−magnification images. Nevertheless, the magnified TEM images shown in Fig. 1f−g show small clusters with a diameter of 0.5–1 nm (highlighted by the red arrows in Fig. 1g), which is consistent with the PXRD results, and these NCs can be clearly observed in the high−angle annular dark–field scanning TEM (HAADF–STEM) images shown in Fig. 1h and Fig. S1. The number of atoms in Ru NCs were estimated as 15–60 based on the diameter of the NCs and cell parameters of Ru. The corresponding elemental mapping results show that B and N were doped into graphene. To further confirm the doping of B, electron energy loss spectroscopy mapping, which is sensitive to light elements, was employed. As shown in Figs. S2 and B was uniformly doped into graphene. Conversely, during pyrolysis, Ru NPs/NG synthesized without H_3BO_3 formed Ru NPs with a much larger size than those formed from Ru NCs/BNG (Fig. S3), and the PXRD pattern of Ru NPs/NG shows much more intense diffraction peaks for metallic Ru (Fig. S4), in accordance with the TEM results. These

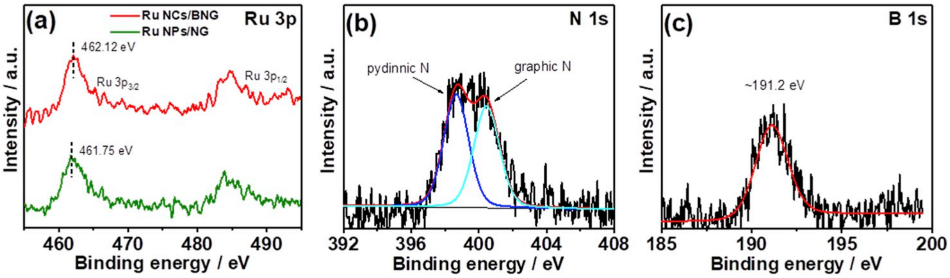

Fig. 2. XPS spectra of (a) Ru 3p in Ru NCs/BNG and Ru NPs/NG, (b) N 1s, and (c) B 1s in Ru NCs/BNG.

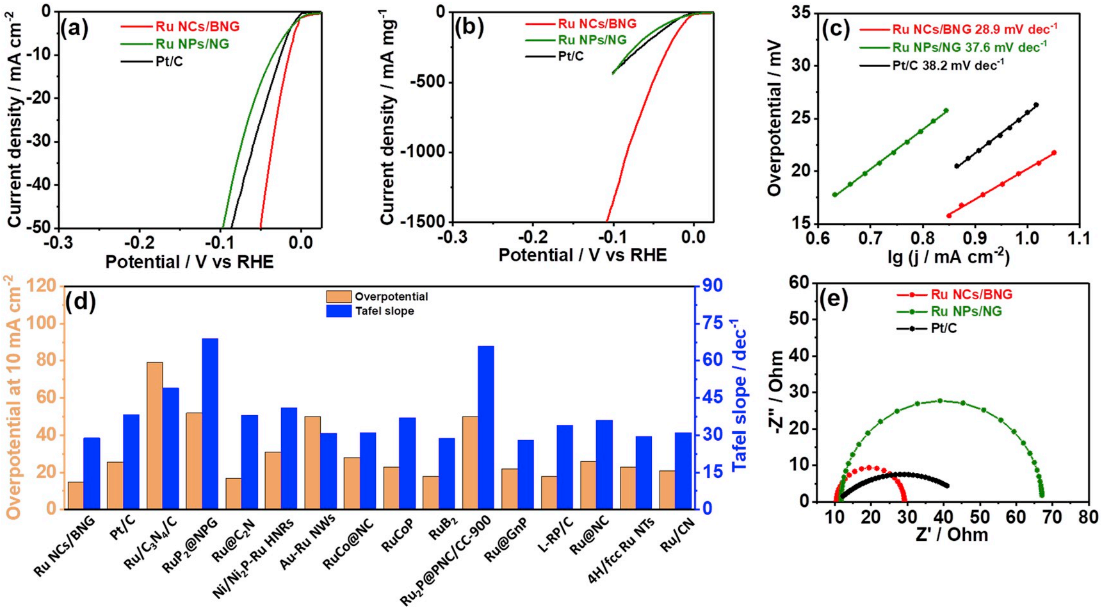

Fig. 3. LSV curves of Ru NCs/BNG, Ru NPs/NG, and Pt/C with current density normalized to (a) the geometry of the electrode and (b) the mass of Ru in 1 M KOH at 2 mV s^{-1} with iR correction; (c) Tafel plots of Ru NCs/BNG, Ru NPs/NG, and Pt/C; (d) histogram of the overpotentials at a current density of 10 mA cm^{-2} and Tafel slopes of Ru NCs/BNG, Pt/C, and other Ru–based catalysts from the literature; and (e) electrochemical impedance spectroscopy (EIS) plots of Ru NCs/BNG, Ru NPs/NG, and Pt/C at an overpotential of 50 mV in 1 M KOH.

results suggest that using H_3BO_3 is crucial for minimizing the size of Ru, and this is the first time that this phenomenon has been observed.

The Ru loading was measured by thermogravimetric analysis (TGA) at atmospheric pressure. The TGA curve of Ru NCs/BNG in Fig. S5 shows a weight loss corresponding to the loss of graphene and a residual mass originating from RuO_2; thus, the residual mass multiplied by the percentage of Ru in RuO_2 (75.9 wt%) represents the Ru loading in Ru NCs/BNG. The mass percentage of Ru NCs/BNG was calculated as ~14.25%, based on the TGA curve. X−ray photoelectron spectroscopy (XPS) was used to further study the components and chemical states of Ru NCs/BNG. The survey spectrum of Ru NCs/BNG shown in Fig. S6a indicates that only C, O, N, Ru, and B are present with no other impurities. Similar results were obtained for Ru NPs/NG (Fig. S7), except for the absence of B. In the C 1s spectrum, the sp [2] hybrid C peak can be clearly observed, indicating that the graphene structure was maintained after pyrolysis (Figs. S6a and S7a). The binding energies of Ru 3p suggest that the metallic Ru was formed, and the positive shift observed for Ru NCs/BNG indicates the electron deficiency of Ru (Fig. 2a). In the N 1s spectrum, N can be divided into pyridinic N and graphenic N, indicating that N was doped into the graphene in Ru NCs/BNG (Fig. 2b) [20–22]. In the B 1s spectrum, the peak at 191.8 eV suggests that B was doped into the graphene in the form of BC_3 (Fig. 2c) [23–25]. The percentage of N and B doped into graphene is 1.38 at% and 0.85 at% determined by the XPS. Raman spectra of graphene, Ru NCs/NG, and Ru NCs/BNG further verified that N and B were doped into graphene during pyrolysis. As shown in Fig. S8, the G band appears around 1580 cm^{-1}; this can be attributed to the E_{2g} mode in graphite and reflects the symmetry and degree of crystallinity of graphitic carbon. The D band arises around 1350 cm^{-1}; this is highly sensitive to the defect−induced peak and can reflect the disorder of the graphite layer. The I_D/I_G ratio of graphene is 0.138, indicating its low defect density, while the I_D/I_G ratios of Ru NCs/NG and Ru NCs/BNG are 1.28 and 1.403, respectively, suggesting that the defects were formed because the coordination numbers of N and B are different from that of C, which verifies that B and N were doped into graphene. Moreover, the electronic conductivity of Ru NCs/BNG and Ru NPs/NG detected by four-probes method is 0.482 and 0.250 Ω cm respectively, which is much lower than that of Pt/C with electronic conductivity of 1.21 Ω cm, this is attributed to the superior electronic conductivity of graphene than that of amorphous carbon, the improved conductivity is benefit to the electrocatalysis.

A series of Ru NCs/BNG compounds with different Ru loadings of 9.03, 14.25, 19.77, and 25.24 wt% (measured by TGA, as shown in Fig. S10) were also synthesized for comparison using the same method as previously described, but with different amounts of Ru precursor. TEM images (Fig. S11−13) suggest that the diameter of the Ru clusters increased with the Ru loading.

3.2. *Electrochemical performances*

3.2.1. *HER activity*

The HER catalytic activities of the series of Ru NCs/BNG compounds were assessed by linear sweep voltammetry (LSV) in 1 M KOH solution at 2 mV s^{-1} after iR correction. As shown in Fig. S14, Ru NCs/BNG with 14.25 wt% Ru present the highest HER activity with a relatively low Ru loading; thus, Ru NCs/BNG with 14.25 wt% Ru were determined as the optimum catalyst and were selected for further studies, described below.

The HER catalytic activities of Ru NCs/BNG, Ru NPs/NG, and commercial 20 wt% Pt/C in 1 M KOH solution are shown in Fig. 3a. Compared with Ru NPs/NG, the HER activity of Ru NCs/BNG was greatly improved by the presence of boron, with a negligible onset potential and the lowest overpotentials of 14 and 50 mV at current densities of 10 and 50 mA cm^{-2}, which even surpasses those of Pt/C at 26 and 86 mV, respectively. To further evaluate the catalytic activity of Ru NCs/BNG, the current densities obtained from LSV curves were normalized to the mass of metal (the Ru loading in Ru NPs/NG was measured as 17.17 wt%, as shown in Fig. S15). As shown in Fig. 3b, Ru NCs/BNG present a much higher mass activity than those of Ru NPs/NG and Pt/C. Moreover, Ru NCs/BNG also presented a higher activity when the catalytic current density was normalized to the number of moles of metal (Fig. S16). As shown in Fig. 3c, Ru NCs/BNG exhibit a Tafel slope of 28.9 mV/dec^{-1}, which is smaller than those of Ru NPs/NG and Pt/C at 37.6 and 38.2 mV dec^{-1}, respectively, indicating that the improved HER kinetics of Ru NCs/BNG were achieved *via* boron doping. Fig. 3d and Table S1 summarize the specific activities and Tafel slopes of state−of−the−art Ru−based catalysts [26–40] and Pt/C, which demonstrate that the catalytic activity of Ru NCs/BNG in alkaline solution is better

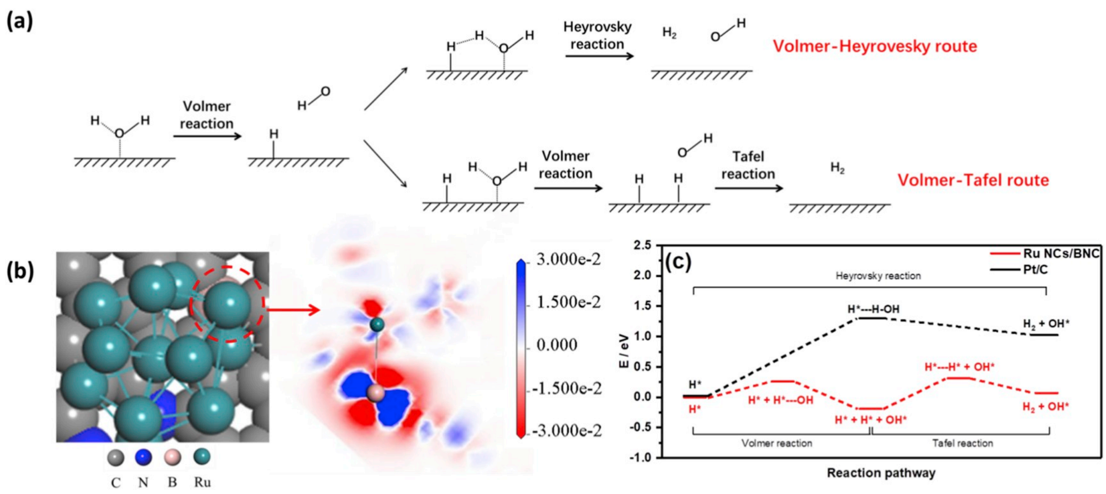

Fig. 4. (a) Scheme showing the mechanisms of the Volmer–Heyrovsky and Volmer–Tafel routes for the HER in alkaline solution; (b) calculation model (top view) and corresponding electronic density difference at the interface highlighted by the red circle; (c) energy diagram of the HER on different surfaces, including the initial, intermediate, final, and additional transition states of the reactants for Ru NCs/BNG and Pt/C.

than those of most state–of–the–art Ru–based catalysts. More importantly, the price of Ru is only 4% that of Pt [27]; thus, the outstanding mass activity of Ru NCs/BNG makes them not only an effective but also a low–cost catalyst for the HER in alkaline solution with excellent potential for replacing Pt in practical applications. Moreover, the electrochemical impedance spectroscopy (EIS) measurements also showed that the HER kinetics were greatly improved after boron doping. The EIS results for Ru NCs/BNG, Ru NPs/NG, and Pt/C are shown in Fig. 3e, and the corresponding circuit model fitting analyses were performed, as shown in Fig. S17 and Table S2. The R_{CT} values follow the order Ru NCs/BNG < Pt/C < Ru NPs/NG, demonstrating that fast electron transfer was realized in Ru NCs/BNG, which also confirms that the reaction kinetics of the active sites were improved by boron doping.

3.2.2. *Origin of HER activity*

Moreover, the effect of boron on improving the HER catalytic activity of Ru NCs/BNG was further discussed.

The mechanism of the HER in alkaline solution is shown in Fig. 4a. The first step involves breaking the H–O bond in H_2O to form the adsorbed H* on the active sites (* represents the active species adsorbed on the active sites of the catalysts), which is called the Volmer reaction (Eq. (1)). The adsorbed H* may then combine with another H atom from water dissociation (called the Volmer–Heyrovsky route, Eqs (1) and (2)) or another adsorbed H* on a neighboring active site (called the Volmer–Tafel route, Eqs (1) and (3)) to produce H_2. The value of the Tafel slope indicates the mechanism and rate–determining step (RDS) of the HER [41–45].

$$H_2O + e^- \rightarrow H^* + OH^- \text{ Volmer reaction, Tafel slope} = 120 \text{ mV dec}^{-1} \quad (1)$$

$$H^* + H_2O + e^- \rightarrow H_2 + OH^- \text{ Heyrovsky reaction, Tafel slope} = 40 \text{ mV dec}^{-1} \quad (2)$$

$$H^* + H^* \rightarrow H_2 \text{ Tafel reaction, Tafel slope} = 30 \text{ mV dec}^{-1} \quad (3)$$

As shown in Fig. 3c, the Tafel slope of Pt/C implies that the HER obeys the Volmer–Heyrovsky route and that the Heyrovsky reaction is the rate–determining equation (RDE), which indicates that the sluggish dissociation of H_2O is the RDS of the HER; these results are consistent with those reported in the literatures [26–32,46,47], and a similar Volmer–Heyrovsky route for Ru NPs/NG was also observed. Nevertheless, the Tafel slope of Ru NCs/BNG suggests that the HER proceeds via the Volmer–Tafel route and that the Tafel reaction is the RDE, indicating that the dissociation of H_2O was boosted by boron doping; thus, the recombination of H* replaced water dissociation to become the RDS. Once the sluggish water dissociation step was accelerated, the overall reaction kinetics of the alkaline HER were promoted, eventually improving the HER catalytic activity of Ru NCs/BNG to surpass that of Pt/C.

To further determine the origin of the above described activity, the HER was performed in acidic solution, where H* adsorption and desorption can be used as the sole activity descriptors, thus directly reflecting the intrinsic catalytic activities of Ru and Pt [9–12]. As depicted in Fig. S18, Pt/C still exhibits the best HER activity in 0.5 M H_2SO_4 but is less efficient in 1 M KOH, indicating that Pt still represents the best intrinsic catalytic activity due to its appropriate H* absorption strength; however, the HER activity of Pt in alkaline solution was encumbered by the sluggish kinetics of water dissociation, so that Pt showed less efficient catalytic kinetics in 1 M KOH. However, the catalytic activity of Ru NCs/BNG in 1 M KOH was similar to that in 0.5 M H_2SO_4 with no obvious degradation. These results indicate that although the intrinsic activity of Ru is inferior to that of Pt, boosting the water dissociation by boron doping can accelerate the alkaline HER kinetics of Ru NCs/BNG, maintaining the catalytic current of Ru NCs/BNG in alkaline solution. Conversely, the HER of Pt/C in alkaline solution was slowed by H_2O dissociation, making its HER activity inferior to that of Ru NCs/BNG. Thus, the improvement in the alkaline HER activity can be mainly attributed to the optimization of the water dissociation barriers, which contributes predominantly to the activity enhancement for the HER in alkaline solution.

To further clarify the above conclusions, DFT was employed to calculate the activation energies of transforming H_2O to H_2 in Ru NCs/BNG and Pt/C. Firstly, the structural optimization revealed that Ru NCs tend to be anchored on B sites to maintain the lowest systemic energy (Fig. S19), indicating that a strong interaction must exist between Ru NCs and B. The electronic density differences in Ru NCs/BNG at the interface between Ru NCs and BNG are shown in Fig. 4b, which shows that the charges are redistributed at the interface, the electrons are transferred from Ru atoms (red region represents electron loss) to B atoms (blue region represents electron accumulation), and the fusiform electron–rich area around B atoms indicates that the electrons from d orbitals of Ru are transferred to the vacant 2p orbitals in the valence shell of B, which is consistent with the XPS results. The electron deficiency of Ru facilitates the nucleophilic attack from H_2O, which induces H–OH bond cleavage, thus accelerating the water dissociation step during the alkaline HER. Secondly, the energy barriers of the alkaline HER were also calculated using DFT. The RDS activation energy differences between Ru NCs/BNG and Pt/C hold the key to their HER

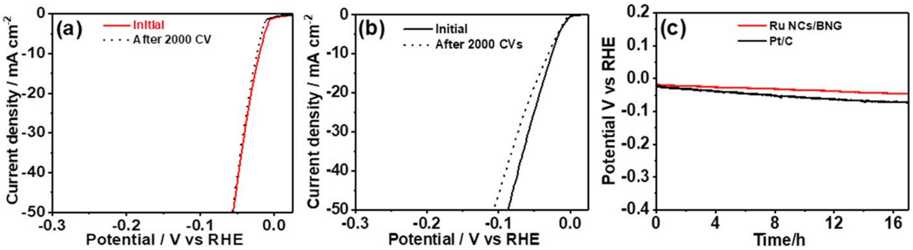

Fig. 5. LSV curves of (a) Ru NCs/BNG and (b) Pt/C before and after 2000 cycles in 1 M KOH at 2 mV s^{-1}, and (c) E–t curves of Ru NCs/BNG and Pt/C in 1 M KOH.

kinetics. Here according to the HER mechanism determined from the Tafel slope, the RDSs of Ru NCs/BNG and Pt/C are the Heyrovsky (Eq. (2)) and Tafel (Eq. (3)) reactions, respectively; thus, the initial Volmer reaction (Eq. (1)) can be neglected in the DFT calculations, and the calculated reaction pathways were started from H*, i.e., the result of the initial Volmer step, and the subsequent RDS energy barriers of Ru NCs/BNG and Pt/C are shown in Fig. 4c (the calculation models are shown in Fig. S20−21). For Pt/C, the energy barrier of the Heyrovsky reaction reached 1.30 eV (125.9 kJ mol^{-1}) due to the sluggish dissociation of H_2O, which significantly slowed the HER kinetics. For Ru NCs/BNG, the energy barrier of the Volmer reaction to form the second H* was as low as 0.26 eV (25.2 kJ mol^{-1}) due to the dissociation of H_2O being greatly accelerated. Subsequently, the energy barrier for recombination of the two adjacent H* (Tafel reaction) is 0.51 eV (49.4 kJ mol^{-1}), which is higher than that of the former Volmer reaction; thus, this becomes the RDS, consistent with the experimental evidence. As shown in Fig. 4c, the general activation energy of Ru NCs/BNG is much lower than that of Pt/C, suggesting higher alkaline HER kinetics for Ru NCs/BNG, even though the intrinsic activity of Ru is inferior to that of Pt, indicating the importance of optimizing the water dissociation barrier in boosting the alkaline HER activity.

3.2.3. *Stability*

Besides the catalytic activity, stability is also an important factor for the HER catalyst. The cycling stabilities of Ru NCs/BNG and Pt/C were evaluated by comparing the LSV curves before and after 2000 cycles (from +0.05 to −0.25 *vs.* RHE at 50 mV s^{-1}) in 1 M KOH solution. As shown in Fig. 5a, Ru NCs/BNG show negligible decay in their catalytic activity, while 20 wt% commercial Pt/C deteriorates significantly (Fig. 5b). To further assess the long−term durability of Ru NCs/BNG and Pt/C, chronopotentiometric measurements were performed at a current density of 10 mA cm^{-2}. The chronopotentiometric curves of Ru NCs/BNG and Pt/C in Fig. 5c suggest that Ru NCs/BNG maintain their catalytic activity with negligible decay during long−term electrolysis, whereas Pt/C does not. After durability testing, Ru NCs maintained good dispersion on graphene in Ru NCs/BNG (Fig. S23), and N, B, and Ru are still dispersed on graphene uniformly (Fig. S24). However, serious agglomeration occurred in Pt/C (Fig. S25). This comparison suggests that Ru NCs/BNG have outstanding stability.

4. Conclusion

In conclusion, Ru NCs anchored on boron and nitrogen−doped graphene (Ru NCs/BNG) were synthesized *via* pyrolyzation of Ru(phen)$_2$Cl$_2$, H_3BO_3, and graphene. During pyrolyzation, boron was not only doped into graphene but also facilitated the formation of ultra−small Ru NCs. The electronic interaction between B and Ru changed the mechanism of the alkaline HER by accelerating cleavage of the H–OH bond, thus lowering the activation energy of the HER, so that the alkaline HER activity of Ru NCs/BNG surpassed that of Pt/C, even though the intrinsic activity of Ru is inferior to that of Pt. This study reveals the importance of the water dissociation barrier with respect to the alkaline HER activity and opens a new avenue for exploring the acceleration of water dissociation through the unique effect of boron.

Author declaration

We wish to confirm that there are known conflicts of interest associated with this publication and there has been no significant financial support for this word that could have influenced its outcome.

Acknowledgements

S.−H.Y, F.−Y.L, and T.−T.X contributed equally to this work. We appreciate the financial support of the National Natural Science Foundation of China (NNSF, 21571131), the Shenzhen Basic Research Layout Project (20170447) and Major Programs for Science and Technology Development of Shenzhen (JSGG20160328151657828, XCL201110060), the major industrial projects of Shenzhen (s2017001850011), and the Key Project of Natural Science Foundation of Guangdong Province (2014A030311028).

Appendix A. Supplementary data

Supplementary data to this article can be found online at https://doi.org/10.1016/j.nanoen.2019.104301.

References

[1] J.K. Norskov, C.H. Christensen, Science 312 (2006) 1322–1323.
[2] I. Roger, M.A. Shipman, M.D. Symes, Nat. Rev. Chem. 1 (2017), 0003.
[3] Z.W. Seh, J. Kibsgaard, C.F. Dickens, I. Chorkendorff, J.K. Nørskov, T.F. Jaramillo, Science 355 (2017) eaad4998.
[4] S. Chu, Y. Cui, N. Liu, Nat. Mater. 16 (2017) 16–22.
[5] J.A. Turner, Science 305 (2004) 972–974.
[6] Z. Zhao, H. Liu, W. Gao, W. Xue, Z. Liu, J. Huang, X. Pan, Y. Huang, J. Am. Chem. Soc. 140 (2018) 9046–9050.
[7] R.D.L. Smith, M.S. Prévot, R.D. Fagan, Z. Zhang, P.A. Sedach, M.K.J. Siu, S. Trudel, C.P. Berlinguette, Science 340 (2013) 60–63.
[8] C.C.L. McCrory, S. Jung, J.C. Peters, T.F. Jaramillo, J. Am. Chem. Soc. 135 (2013) 16977–16987.
[9] G. Zhang, G. Wang, Y. Liu, H. Liu, J. Qu, J. Li, J. Am. Chem. Soc. 138 (2016) 14686–14693.
[10] H. Jin, X. Liu, Y. Jiao, A. Vasileff, Y. Zheng, S.-Z. Qiao, Nano Energy 53 (2018) 690–697.
[11] Y. Jiao, Y. Zheng, K. Davey, S.-Z. Qiao, Nat. Energy 1 (2016) 16130.
[12] Y. Jiao, Y. Zheng, M. Jaroniec, S.Z. Qiao, Chem. Soc. Rev. 44 (2015) 2060–2086.
[13] Y. Zheng, Y. Jiao, A. Vasileff, S.-Z. Qiao, Angew. Chem. Int. Ed. 57 (2018) 7568–7579.
[14] R. Subbaraman, D. Tripkovic, K.-C. Chang, D. Strmcnik, A.P. Paulikas, P. Hirunsit, M. Chan, J. Greeley, V. Stamenkovic, N.M. Markovic, Nat. Mater. 11 (2012) 550–557.
[15] I. Ledezma-Yanez, W.D.Z. Wallace, P. Sebastián-Pascual, V. Climent, J.M. Feliu, M.T.M. Koper, Nat. Energy 2 (2017) 17031.
[16] M.D. Segall, P.J.D. Lindan, M. Probert, C.J. Pickard, P.J. Hasnip, S.J. Clark, M.C. J. Payne, J. Phys. Condens. Matter 14 (2002) 2717–2744.
[17] J.P. Perdew, K. Burke, M. Ernzerhof, Phys. Rev. Lett. 77 (1996) 3865–3868.
[18] D.R. Hamann, M. Schlüter, C. Chiang, Phys. Rev. Lett. 43 (1979) 1494–1497.
[19] D. Voiry, H. Yamaguchi, J. Li, R. Silva, D.C.B. Alves, T. Fujita, M.W. Chen, T. Asefa, V. Shenoy, G. Eda, M. Chhowalla, Nat. Mater. 12 (2013) 850–855.
[20] H. Tabassum, W. Guo, W. Meng, A. Mahmood, R. Zhao, Q. Wang, R. Zou, Adv. Energy Mater. 5 (2017) 1601671.
[21] H. Yan, Y. Xie, Y. Jiao, A. Wu, C. Tian, X. Zhang, L. Wang, H. Fu, Adv. Mater. 1 (2018) 1704156.
[22] Y. Han, Y.-G. Wang, W. Chen, R. Xu, L. Zheng, J. Zhang, J. Luo, R.-A. Shen, Y. Zhu, W.-C. Cheong, others, J. Am. Chem. Soc. 139 (2017) 17269–17272.
[23] M. Chhetri, S. Maitra, H. Chakraborty, U.V. Waghmare, C.N.R. Rao, Energy Environ. Sci. 9 (2016) 95–101.

[24] Z.-S. Wu, A. Winter, L. Chen, Y. Sun, A. Turchanin, X. Feng, K. Müllen, Adv. Mater. 24 (2012) 5130–5135.
[25] C.H. Choi, S.H. Park, S.I. Woo, ACS Nano 6 (2012) 7084–7091.
[26] Y. Zheng, Y. Jiao, Y. Zhu, L.H. Li, Y. Han, Y. Chen, M. Jaroniec, S.-Z. Qiao, J. Am. Chem. Soc. 138 (2016) 16174–16181.
[27] Z. Pu, I.S. Amiinu, Z. Kou, W. Li, S. Mu, Angew. Chem. Int. Ed. 56 (2017) 11559–11564.
[28] J. Mahmood, F. Li, S.-M. Jung, M.S. Okyay, I. Ahmad, S.-J. Kim, N. Park, H. Y. Jeong, J.-B. Baek, Nat. Nanotechnol. 12 (2017) 441–446.
[29] Y. Liu, S. Liu, Y. Wang, Q. Zhang, L. Gu, S. Zhao, D. Xu, Y. Li, J. Bao, Z. Dai, J. Am. Chem. Soc. 140 (2018) 2731–2734.
[30] Q. Lu, A.-L. Wang, Y. Gong, W. Hao, H. Cheng, J. Chen, B. Li, N. Yang, W. Niu, J. Wang, Y. Yu, X. Zhang, Y. Chen, Z. Fan, X.-J. Wu, J. Chen, J. Luo, S. Li, L. Gu, H. Zhang, Nat. Chem. 10 (2018) 456–461.
[31] J. Su, Y. Yang, G. Xia, J. Chen, P. Jiang, Q. Chen, Nat. Commun. 8 (2017) 14969.
[32] J. Xu, T. Liu, J. Li, B. Li, Y. Liu, B. Zhang, D. Xiong, I. Amorim, W. Li, L. Liu, Energy Environ. Sci. 11 (2018) 1819–1827.
[33] Q. Li, X. Zou, X. Ai, H. Chen, L. Sun, X. Zou, Adv. Energy Mater. 9 (2018) 1803369.
[34] T. Liu, B. Feng, X. Wu, Y. Niu, W. Hu, C.M. Li, ACS Appl. Energy Mater. 1 (2018) 3143–3150.
[35] F. Li, G.-F. Han, H.-J. Noh, I. Ahmad, I.-Y. Jeon, J.-B. Baek, Adv. Mater. 30 (2018) 1803676.
[36] J. Yu, Y. Guo, S. She, S. Miao, M. Ni, W. Zhou, M. Liu, Z. Shao, Adv. Mater. 30 (2018) 1800047.
[37] Z.-L. Wang, K. Sun, J. Henzie, X. Hao, C. Li, T. Takei, Y.-M. Kang, Y. Yamauchi, Angew. Chem. Int. Ed. 57 (2018) 5848–5852.
[38] Q. Lu, A.-L. Wang, H. Cheng, Y. Gong, Q. Yun, N. Yang, B. Li, B. Chen, Q. Zhang, Y. Zong, L. Gu, H. Zhang, Small 14 (2018) 1801090.
[39] J. Zhang, P. Liu, G. Wang, P.P. Zhang, X.D. Zhuang, M.W. Chen, I.M. Weidinger, X. L. Feng, J. Mater. Chem. A 5 (2017) 25314–25318.
[40] Q. Hu, G. Li, Z. Han, Z. Wang, X. Huang, X. Chai, Q. Zhang, J. Liu, C. He, Adv. Energy Mater. 9 (2019) 1901130.
[41] W. Li, Y. Liu, M. Wu, X. Feng, S.A.T. Redfern, Y. Shang, X. Yong, T. Feng, K. Wu, Z. Liu, B. Li, Z. Chen, J.S. Tse, S. Lu, B. Yang, Adv. Mater. 30 (2018) 1800676.
[42] J. Wang, F. Xu, H. Jin, Y. Chen, Y. Wang, Adv. Mater. 29 (2017) 1605838.
[43] E. Skúlason, V. Tripkovic, M.E. Björketun, S. Gudmundsdóttir, G. Karlberg, J. Rossmeisl, T. Bligaard, H. Jónsson, J.K. Nørskov, J. Phys. Chem. C 114 (2010) 18182–18197.
[44] J. Yan, L. Kong, Y. Ji, Y. Li, J. White, S. (Frank) Liu, X. Han, S.-T. Lee, T. Ma, Commun. Chem. 1 (2018) 95.
[45] C.-T. Dinh, A. Jain, F.P.G. de Arquer, P.D. Luna, J. Li, N. Wang, X. Zheng, J. Cai, B. Z. Gregory, O. Voznyy, B. Zhang, M. Liu, D. Sinton, E.J. Crumlin, E.H. Sargent, Nat. Energy 4 (2019) 107–114.
[46] Q. Hu, X. Liu, B. Zhu, L. Fan, X. Chai, Qi Zhang, J. Liu, C. He, Z. Lin, Nano Energy 50 (2018) 212–219.
[47] Q. Hu, G. Li, G. Li, X. Liu, B. Zhu, X. Chai, Q. Zhang, J. Liu, C. He, Adv. Energy Mater. 9 (2019) 1803867.